ACS NANO
Cite This: ACS Nano 2019, 13, 13169–13175
www.acsnano.org

ARTICLE

Edge Contact for Carrier Injection and Transport in MoS_2 Field-Effect Transistors

Homin Choi,[†,‡,§] Byoung Hee Moon,[*,†,§] Jung Ho Kim,[†,‡] Seok Joon Yun,[†,‡] Gang Hee Han,[†] Sung-gyu Lee,[†,‡] Hamza Zad Gul,[†,‡] and Young Hee Lee[*,†,‡]

[†]Center for Integrated Nanostructure Physics, Institute for Basic Science, Sungkyunkwan University, Suwon 16419, Korea
[‡]Department of Energy Science, Department of Physics, Sungkyunkwan University, Suwon 16419, Korea

Supporting Information

ABSTRACT: **The contact properties of van der Waals layered semiconducting materials are not adequately understood, particularly for edge contact. Edge contact is extremely helpful in the case of graphene, for producing efficient contacts to vertical heterostructures, and for improving the contact resistance through strong covalent bonding. Herein, we report on edge contacts to MoS_2 of various thicknesses. The carrier-type conversion is robustly controlled by changing the flake thickness and metal work functions. Regarding the ambipolar behavior, we suggest that the carrier injection is segregated in a relatively thick MoS_2 channel; that is, electrons are in the uppermost layers, and holes are in the inner layers. Calculations reveal that the strength of the Fermi-level pinning (FLP) varies layer-by-layer, owing to the inhomogeneous carrier concentration, and particularly, there is negligible FLP in the inner layer, supporting the hole injection. The contact resistance is large despite the significantly reduced contact resistivity normalized by the contact area, which is attributed to the current-crowding effect arising from the narrow contact area.**

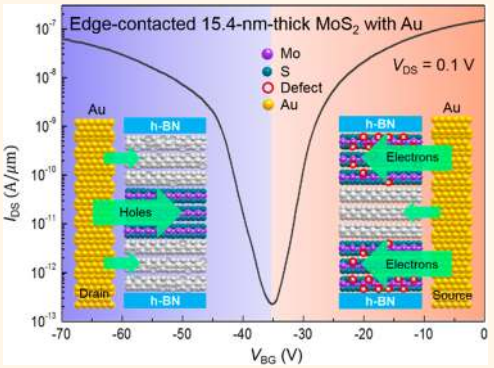

KEYWORDS: *Fermi-level pinning, edge contact, ambipolar characteristics, MoS_2 field-effect transistor, negative Schottky barrier height, mobility, current crowding*

Among the several types of transition-metal dichalcogenides (TMDs), semiconducting TMDs have attracted considerable interest, particularly for high-performance transistors because they are potential alternatives to graphene.[1−4] However, achieving ohmic metal contact to two-dimensional (2D) semiconducting TMDs has been challenging, in contrast to metal contacts to graphene and conventional bulk semiconductors.[5−8] The contact resistance of graphene devices has been reduced *via* strong covalent bonds between metals and the graphene edge.[1,9] This edge contact is recognized as an extremely effective method for fabricating graphene devices having vertically stacked heterostructures.[10,11] Meanwhile, this approach is unfavorable for monolayer TMDs owing to the current-crowding effect caused by the large transfer length.[12] Thus, the edge contact to multilayer TMDs[13] is expected to be beneficial owing to the larger contact area and higher mobility compared with the contact to a monolayer. However, systematic experimental studies on this type of contact, such as for various thicknesses, are scarce.

Another issue regarding edge contact is the Fermi-level pinning (FLP) effect. The metal contact to the top of MoS_2 films (TCM) exclusively exhibits n-type characteristics, with a Schottky barrier weakly dependent on the metal work function.[6,14,15] This is attributed to the strong FLP close to the charge-neutrality level of the interface gap states in MoS_2, which are located near the conduction-band minimum. Interface gap states can be understood according to several mechanisms, such as metal-induced gap states,[16] defects,[17,18] and chemical bonds.[19,20] Charge transfer occurs between metal and interface states, forming interface dipoles. The final band diagram is determined by the band bending caused by the charge transfer due to the difference in the Fermi levels of the metal and semiconductor bulk, together with the interface dipole field.

In the edge contact to MoS_2 (ECM), the charge transfer at the interface with the metal is expected to be dominated by the chemical bonds. Stronger bonding generally indicates greater charge transfer, *i.e.*, a stronger FLP effect. However, the main restriction on the charge transfer in the edge contact is the small contact area. Because the interface dipoles are localized near the interface, *e.g.*, within a distance equal to the length of a

Received: August 1, 2019
Accepted: November 12, 2019
Published: November 12, 2019

Downloaded via SUNGKYUNKWAN UNIV on November 28, 2019 at 01:53:35 (UTC).
See https://pubs.acs.org/sharingguidelines for options on how to legitimately share published articles.

© 2019 American Chemical Society

DOI: 10.1021/acsnano.9b05965
ACS Nano 2019, 13, 13169–13175

few atoms, the dipole field confined in the small area decays rapidly.[21] In this case, the FLP effect on the band bending significantly depends on the depletion width due to space charges. In this article, we report on the charge transport through the edge contact of various metals to a MoS_2 channel with various thicknesses. As the thickness of the MoS_2 channel increases, ambipolar behavior is clearly observed in the MoS_2 device with an edge contact of a high-work-function metal, for example, Au. We propose that the depletion widths and FLP effects govern the carrier transport in three regimes of multilayer MoS_2: electrons in the top layers near the surface, holes in the inner layers, and electrons in the bottom layers near the substrate.

RESULTS AND DISCUSSION

Figure 1a shows a device schematic for the edge contact to MoS_2. The exfoliated MoS_2 is sandwiched between two 10–20-nm-thick hexagonal boron nitride (h-BN) films on a 300-nm-thick SiO_2/Si substrate. The contact area defined *via* electron-beam (e-beam) lithography is etched using SF_6 plasma to expose the edge of MoS_2. The e-beam patterns for the metal deposition are made again on fresh poly(methyl methacrylate) (PMMA), followed by the deposition of metals in a high vacuum of $\sim 10^{-6}$ Torr. The carrier injection from the MoS_2 surface is eliminated through h-BN passivation on the MoS_2 channel, enabling exclusive investigation of the edge contact effect. Figure 1b and c show the transfer characteristics (drain–source current, I_{DS} *vs* back-gate bias, V_{BG}) for the ECM with several thicknesses of two contact metals: Mn/Au (low work function, Φ_M = 4.1 eV) and Au (high work function, Φ_M = 5.1 eV) (see Supplementary Note 1 and Figure S1 for the oxidation issue). The thicknesses of the deposited metals are 10 nm/60 nm for Mn/Au and 70 nm for Au. The ECM with Mn/Au (Figure 1b) exhibits n-type characteristics for samples up to ~10 nm thick, similar to all the top-contacted devices (see Supplementary Figure 2) and to previously reported devices.[6] This is ascribed to the work function of Mn (4.1 eV), which is located near the electron affinity[22] or conduction-band minimum in the multilayer MoS_2 (χ = 4.0 eV) regardless of the FLP effect.

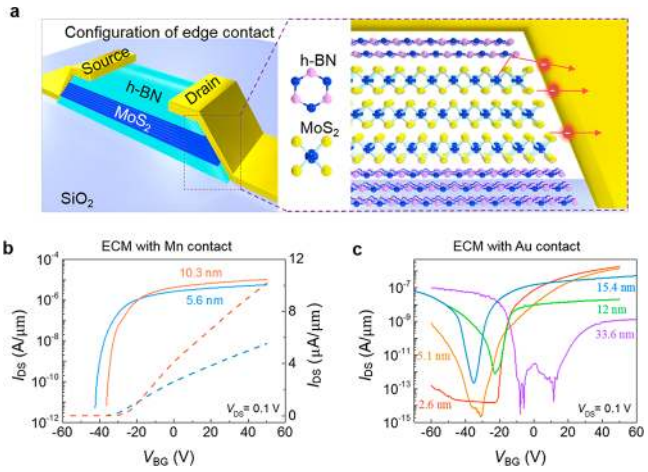

Figure 1. Device structure and transfer characteristics for edge-contacted MoS_2 with various thicknesses and metals. (a) Schematic of the edge-contacted multilayer MoS_2. The right-side figure shows how carriers flow in the devices. (b, c) I_{DS}–V_{BG} characteristics of the (b) Mn/Au- and (c) Au-edge-contacted multilayer MoS_2 devices with different thicknesses of MoS_2 at room temperature. The left and right axes in (b) correspond to logarithmic and linear scales, respectively.

In contrast, the ECM with Au (Figure 1c) exhibits n-type behavior at a thickness below 3 nm, but an ambipolar feature starts to emerge. The device exhibits prominent ambipolar behavior for a flake thickness greater than ~10 nm. Because the field penetration depth is experimentally estimated to be ~50 nm in MoS_2 devices,[23] the switching behavior of MoS_2 devices with a thickness of <50 nm is well controlled by the back-gate bias through ~300-nm-thick SiO_2. As we discuss later in more detail, the dominant carrier transport in Figure 1c—either holes or electrons—can be controlled by changing not only the thickness of the flakes but also the contact or channel quality during the device fabrication (see Supplementary Note 2 and Figure S3). Similar ambipolar characteristics are also observed with a relatively weak p-type behavior for the ECM with Cr (moderate work function, Φ_M = 4.5 eV) (see Supplementary Figure 4). This differs from the results for the top-contacted MoS_2 with Au, which exhibits n-type characteristics even for 15.4-nm-thick samples (Figure S2c).

Ambipolar field-effect transistors with top-contacted MoS_2 have been demonstrated *via* strong gating using an ion gel[24] or extrinsic carrier conversion using chemical doping.[25,26] However, such devices are unlikely to exhibit carrier conversion in a device of highly n-doped MoS_2 on 300-nm-thick SiO_2 as a dielectric, within the experimental back-gate bias range. To explain the ambipolar behavior of our ECM, we first note that carriers are injected inhomogeneously owing to the different carrier densities within the layers.[27−29] According to our experimental results (Figures 1c and S2c), the p-type transport occurs only in a thick ECM with Au contacts, but not in a thin ECM or in a TCM of any thickness. Thus, we suggest the existence of weakly n-doped or intrinsic layers in the middle of the multilayer MoS_2, while the top layers are n-doped.[27] If all the layers are highly n-doped, p-type transport is improbable owing to the high built-in potential (or effective Schottky barrier height for holes), regardless of the FLP effect.

Figure 2 presents schematics of a proposed model for the ambipolar characteristics with one of the transfer curves in Figure 1c. The left and right insets show the situations of hole injection (V_{BG} < −35 V) in the inner layers and electron injection in both the top and bottom layers (V_{BG} > −35 V), respectively. The corresponding band diagrams are shown in the left and right figures, without consideration of the FLP effect in the thermal equilibrium state. As we discuss later in more detail, the inner layer is nearly intrinsic; hence, the depletion width is so large that the local pinning dipole charges are incapable of modulating the Schottky barrier height (or band bending *via* space charges), thus supporting hole injection. As the flake thickness increases, the hole transport tends to be enhanced, as shown in Figure 1c, likely owing to the reduced effects of the substrate or surface scattering.

Because the doped electron concentrations in both the top and bottom layers are high because of defects resulting from the exposure to air during device fabrication,[27] the depletion width is small. Thus, electron tunneling is more favorable than thermionic hole emission, even in the case of weak FLP, because the barrier height for holes is too high to be overcome, owing to the high built-in potential.

We now discuss the FLP effect in the ECM and TCM. Figure 3a presents schematics of electric dipoles due to the interface states and the corresponding potential V_{dipole} for the

DOI: 10.1021/acsnano.9b05965
ACS Nano 2019, 13, 13169−13175

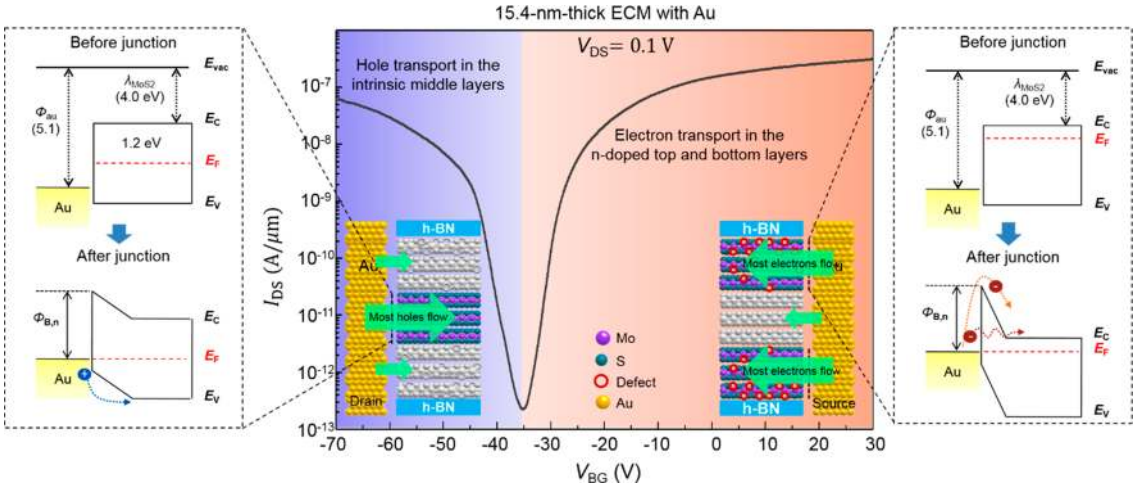

Figure 2. Schematics of carrier injection at the edge of MoS_2 with a Au contact. I_{DS}−V_{BG} ambipolar transfer characteristics for a 15.4-nm-thick ECM with Au (shown in Figure 1c). The blue and red regions indicate p-type and n-type characteristics, respectively. The purple-blue (colored) and white atoms in the inset describe major and minor channels for selective carrier injection depending on the back-gate bias. The band diagrams without the FLP effect of the junctions are presented in the dashed-line boxes on the left and right for the hole and electron injections, respectively.

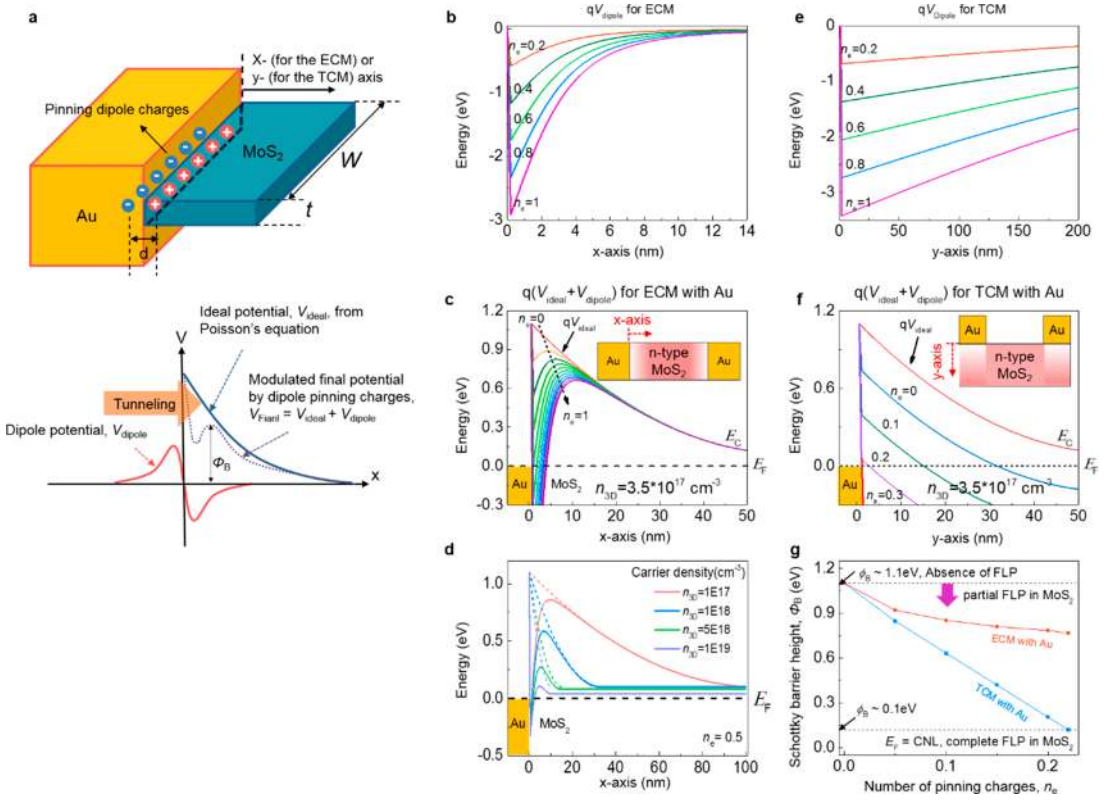

Figure 3. Calculation of the FLP. (a) Schematic of dipole formation in the metal−semiconductor contact and potential profiles. (b, e) Dipole potentials; V_{dipole} at various n_e for ECM (b) and TCM (e). (c, f) Resulting final potentials (or Schottky barriers) V_{final} at different n_e values and n_{3D} = 3.5 × 10^{17} cm^3 for the ECM (c) and TCM (f). The insets in (c) and (f) define the *x*-axis for the ECM and TCM, respectively. (d) V_{ideal} (dashed lines) and V_{final} (solid lines) for different n_{3D} values at n_e = 0.5. (g) Plot of the Schottky barrier height for the TCM and ECM with respect to n_e at n_{3D} = 3.5 × 10^{17} cm^3. When n_e = 0.22 in the TCM, the Fermi level is perfectly pinned to the charge-neutrality level.

Au contact with the edge of MoS_2. Here, the final modulated potential is $V_{Final} = V_{ideal} + V_{dipole}$ (see Supplementary Note 3 for the calculation methods). V_{ideal} represents the potential or band-bending profile resulting from the Fermi-level difference between the metal and the semiconductor, without consideration of any defect or interface states. The FLP is the effect whereby V_{ideal} is modulated by V_{diople} so that the Fermi level becomes aligned with the charge-neutrality level, resulting in the deviation of the Schottky barrier height from the Schottky−Mott rule. Thus, a larger amount of charge transfer between the interface states and the metal generally corresponds to stronger FLP.[30] Here, we expect a higher transferred charge density (or density of interface dipoles) in the ECM than in the TCM owing to the chemical bonding at

DOI: 10.1021/acsnano.9b05965
ACS Nano 2019, 13, 13169−13175

the edges. However, the dipole potential V_{dipole} of the ECM decreases rapidly with the increasing distance from the contact, as the dipole distribution is confined by the sample thickness; that is, the dipole potential is produced by two oppositely charged parallel sheets with a sample contact width W and thickness t. If the Schottky barrier width or depletion width (W_d) formed by the charge transfer due to the Fermi-level difference between the metal and the semiconductor bulk is too large for the potential range caused by interface dipoles, the modulation of the Schottky barrier by V_{dipole} is minor. Thus, the Fermi level at the edge is not sufficiently pulled toward the charge-neutrality level; that is, the FLP effect is weak.

To investigate the behavior of V_{dipole}, we used d = 0.32 nm (approximately the diameter of one atom) for the separation of two charge plates[31] and t = 10 nm. We define n_e as the average number of pinning charges (dipoles) per bond between Au and S atoms for both the ECM and TCM. Figure 3b shows the V_{dipole} of the ECM with various values of n_e, which decays quickly, reaching a value of <50 meV near 15 nm. The modulation of V_{ideal} by V_{dipole} above this range, *i.e.*, 15 nm, is very weak when the depletion width, W_d, is significantly larger than 15 nm. The modulation of V_{ideal} in this case is shown in Figure 3c for various n_e values. We consider, for example, the depletion width or the carrier density at zero gate bias, where no extrinsic doping effect is included. We assume $W_d \approx 50$ nm, corresponding to the volume carrier density $n_{3D} = 3.5 \times 10^{17}$cm^{-3} ($n_{2D} \approx n_{3D}t = 3.5 \times 10^{11}$ cm^{-2} is the areal density corresponding to the threshold voltage $V_{th} \approx -5$ V for the 300-nm-thick SiO_2 dielectric, according to $n_{2D} = \frac{C_{ox}}{q}(V_{BG}(=0) - V_{th})$, where C_{ox} represents the dielectric capacitance). As n_e increases, the modification in V_{ideal} is significant for x < 10 nm but weak for x > 10 nm, resulting in a high Schottky barrier even for the fairly large n_e = 1 (Figure 3c). This indicates that the FLP effect is partial only for a large W_d (depletion width).

For a larger n_{3D}, W_d is smaller; thus, the FLP effect becomes stronger. Figure 3d shows this trend for various n_{3D} values at n_e = 0.5. Here, the dashed and solid lines correspond to V_{ideal} and V_{Final}, respectively, for different n_{3D} values. Nearly complete FLP occurs at $n_{3D} = 1.0 \times 10^{19}$ cm^{-3} ($W_d \approx 10$ nm), where the Fermi level of MoS_2 is close to the charge-neutrality level. Because this value corresponds to $V_{th} \approx -140$ V, which is significantly higher than the value typically observed for experimental devices, only moderate partial pinning occurs at the practical carrier density, for example, at $n_{3D} = 1.0 \times 10^{18}$ cm^{-3} ($V_{th} \approx -14$ V). This potentially indicates a considerable FLP effect for the heavily n-doped top and bottom layers and a weak FLP effect for the weakly n-doped or intrinsic middle layers, which provides greater flexibility of metals for hole injection (see Supplementary Figure 5 for the band-bending profile of the intrinsic layer).

We considered the FLP effect for the TCM as well, for comparison. The main difference from the ECM is the larger contact area. We used the transfer length $L_T = 1$ μm for the contact length, which is significantly larger than that (10 nm) for the edge contact. Although we expected a smaller value of n_e compared with the case of the edge contact because of the absence of dangling bonds,[2] a recent study indicated that defects can be generated during the metal evaporation, resulting in an enhancement in the charge transfer and the FLP effect.[18] Additionally, the shortest bonding length of the top contact is theoretically comparable to that of the edge contact.[32] Thus, the n_e for the top contact may not be significantly smaller than that for the edge contact. Figure 3e shows V_{dipole} for various n_e values in the TCM. The potential decreases far more slowly than that in the case of the edge contact (Figure 3b), because of the significantly larger contact length. The corresponding V_{Final} is shown in Figure 3f at $n_{3D} = 3.5 \times 10^{17}$ cm^{-3}, which is the same density as in Figure 3c. The Schottky barrier height decreases significantly as n_e increases. We compare the Schottky barrier height for the ECM and TCM with respect to n_e at the same carrier density, *i.e.*, $n_{3D} = 3.5 \times 10^{17}$ cm^{-3}, as shown in Figure 3g (see Supplementary Figure S6 for the V_{Final} for each n_e value). The perfect FLP for the TCM is observed at $n_e \approx 0.28$, where the Fermi level of MoS_2 is perfectly aligned with the charge-neutrality level. In this top contact, carriers must always traverse the heavily n-doped top layers with strong FLP, leading to exclusively n-type characteristics (see Supplementary Note 4 and Figure S7 for additional details).

To further analyze the charge-injection behavior, we measured the transfer characteristics of the ECM at different temperatures. According to the thermionic emission theory for 2D nanosheets, I_{DS} is expressed as[33−35]

$$I_{DS} = AA^*T^{1.5} \exp\left[-\frac{q}{k_B T}\left(\phi_B - \frac{V_{DS}}{n}\right)\right] \quad (1)$$

where A represents the area of current injection; A^* represents the Richardson constant; n represents the ideality factor; V_{DS} represents the drain−source voltage; k_B represents the Boltzmann constant; and ϕ_B represents the Schottky barrier height. We measured 6-nm-thick multilayer MoS_2 with a Mn/Au contact. In this case, the work function of Mn (~4.1 eV) is close to the presumed charge-neutrality level of MoS_2; thus, the FLP was expected to have a negligible effect on the final Schottky barrier height. Figure 4a shows the transfer characteristics at V_{DS} = 0.1 V, which were measured from

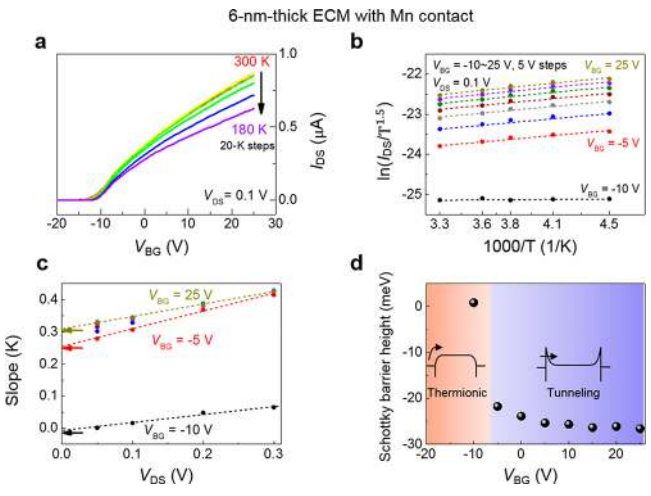

Figure 4. Extraction of the Schottky barrier height for a 6-nm-thick ECM with Mn. (a) Transfer characteristics at V_{DS} = 0.1 V for different temperatures. (b) Arrhenius plot ln($I_{DS}/T^{3/2}$) *vs* 1000/T for various gate biases (V_{BG}). (c) Extraction of ϕ_B *via* the *y*-intercept values, *i.e.*, zero V_{DS} limit. (d) Obtained Schottky barrier heights ϕ_B with respect to the gate bias. The band diagrams in the red and blue regions correspond to the thermionic and tunneling emission, respectively.

DOI: 10.1021/acsnano.9b05965
ACS Nano 2019, 13, 13169−13175

300 to 180 K, in 20 K steps. The barrier height was extracted from the Arrhenius plot, *i.e.*, $\ln(I_{DS}/T^{3/2})$ *vs* the reciprocal of the temperature $(1000/T)$, for various V_{BG} values at several V_{DS} values. Figure 4b shows the plots for V_{DS} = 0.1 V. The slope in this figure is expressed as $-\left(\frac{q}{1000k_B}\right)\left[\phi_B - \frac{V_{DS}}{n}\right]$. The slopes were plotted with respect to V_{DS}, and the effective Schottky barrier height was extracted from the *y*-intercept $S_0 = -\left(\frac{q\phi_B}{1000k_B}\right)$, as shown in Figure 4c. Finally, we plotted the Schottky barrier height obtained in this manner for several different V_{BG} values, as shown in Figure 4d. Interestingly, the Schottky barrier height is negative for most ranges of V_{BG} (the similar result for edge-contacted monolayer MoS_2 with Au is shown in Supplementary Figure S8). In general, the Schottky barrier height determined using eq 1 decreases as V_{BG} increases, because the Schottky barrier becomes lower and thinner, and the tunneling effect prevails over the thermionic emission, reducing the temperature dependence of the current; this leads to a negative value for a high V_{BG}.[36] The range of V_{BG} for the negative Schottky barrier height in the ECM is far broader than that in the TCM. However, the different additional effects for this tunneling-like behavior cannot be excluded, as described in the next section.

Figure 5a shows a comparison of the normalized contact resistance R_cW for the ECM and TCM at two drain−source

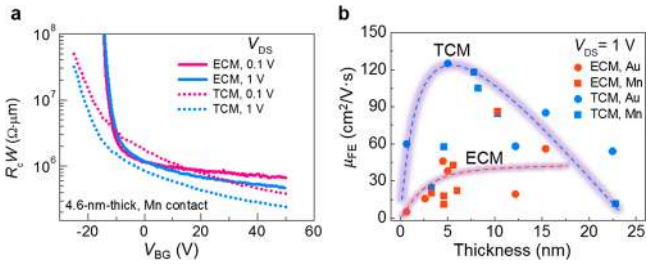

Figure 5. Contact resistance and mobility of the ECM and TCM. (a) Contact resistance of the ECM and TCM at drain biases of 0.1 and 1 V with respect to V_{BG} for 4.6-nm-thick samples. V_{BG} was adjusted by subtracting the threshold voltages. (b) Two-probe field-effect mobility (μ_{FE}) of edge- and top-contacted devices with various thicknesses and metal electrodes. Red circles: ECM with Au contact; red squares: ECM with Mn contact; blue circles: TCM with Au contact; blue squares: TCM with Mn contact.

voltages: V_{DS} = 0.1 and 1 V. The contact resistance, R_c, is obtained as $R_c = (R_T - R_{Sh})/2$, where $R_T = V_{DS}/I_{DS}$ and $R_{Sh} = (V_{in}/I_{DS})(L_{out}/L_{in})$. R_T, R_{Sh}, V_{in}, L_{out}, and L_{in} represent the total resistance, sheet resistance, voltage drop through the inner electrodes, channel length between the source/drain, and channel length between the two inner electrodes, respectively. Two devices were fabricated from the same ∼4.6-nm-thick flake with a Mn contact. For the TCM, R_cW is significantly smaller for V_{DS} = 1 V over the entire range of V_{BG}, which is consistent with the Schottky barrier. In contrast, R_cW for the ECM is almost independent of V_{DS} for the subthreshold region, *i.e.*, $V_{BG} \lesssim 5$ V, although similar behavior is observed for the TCM at a higher V_{BG}. Because of the large contact resistance of the ECM, the two-probe field-effect electron mobility μ_{FE} of the ECM at V_{DS} = 1 V is lower than that of the TCM, up to a film thickness of ∼20 nm for both metal contacts (Au and Mn), as shown in Figure 5b. Here, $\mu_{FE} = \frac{L}{W}\frac{G_m}{C_{ox}}\frac{1}{V_{DS}}$, where L and G_m represent the channel length and transconductance (defined as $G_m = dI_{DS}/dV_{GS}$), respectively. As the flake thickness increases to 5 nm, μ_{FE} increases for both the ECM and TCM, because the bottom layers screen the impurity charges at the interface between the sample and the substrate. However, the μ_{FE} for the TCM decreases with an increase in the larger film thickness to ≥5 nm owing to the interlayer resistance.[37] The contact resistivity ρ_c normalized by the contact area A, *i.e.*, $\rho_c \equiv R_c \times A$, is approximately 2 orders of magnitude lower for the ECM than for the TCM (see Supplementary Figure S9). The trade-off of the mobility and resistivity between the ECM and the TCM can be explained by the current-crowding effect. This effect occurs because most currents are injected into the material within a transfer length L_T determined by the ratio of the contact resistivity to the sheet resistivity.[38] If the charge-injection length is smaller than the transfer length, the contact resistance R_c increases, as in the case of the ECM.

CONCLUSION

We investigated the carrier injection of the ECM devices with different flake thicknesses and different metal electrodes. We found that the carrier type of the edge-contacted multilayer MoS_2 transistor could be controlled by depositing metals with different work functions, in contrast to the TCM transistor. To explain the more prominent ambipolar behavior in thicker ECM with a high work function metal (Au), we proposed a model for the charge distribution within layers and the carrier injection through the junction at the edge. This model differs from the previous models,[28,29] in which n-doping due to the exposure of samples to the air environment is not considered. A uniform carrier distribution is assumed before gating; thus, the ambipolar behavior only in a thick ECM is not adequately explained. We also demonstrated from the calculations that the FLP strongly depends on the depletion width and the carrier density. Because of the inhomogeneous charge distribution, the strength of the FLP varies layer-by layer, yielding significant FLP in the top and bottom layers and negligible FLP in the middle layers; this enhances the tunability for hole injection with various metal contacts. Further, the calculations indicated that the FLP effect in the ECM is weaker than that in the TCM owing to the smaller contact area. Even for the top contact, if the top layers keep from external n-doping, a p-type characteristics can be achieved *via* Fermi-level depinning.[18] The large contact resistance in the ECM is attributed to the smaller contact length relative to the transfer length, which mainly limits the two-probe field-effect mobility. However, the mobility crossover at a ∼20 nm thickness between the edge and top contacts suggests the superiority of edge contacts over top contacts for thicker samples.

METHODS

Device Fabrication. Multilayer MoS_2 was exfoliated using the Scotch-tape micromechanical cleavage technique, and the monolayer MoS_2 used in this study was grown *via* chemical vapor deposition. MoS_2 was transferred onto the prepared h-BN (10−20 nm) films, which were already mechanically exfoliated on SiO_2 (300 nm)/Si (500 μm) substrates. Next, the exfoliated 10−20-nm-thick h-BN films were transferred to the top of MoS_2 to form h-BN/MoS_2/h-BN heterostructures for edge-contacted devices (see Supplementary Figure S10 for schematics of the device fabrication). For top-contacted devices, we used MoS_2 regions that were not covered by top h-BN films. The samples were spin-coated with PMMA and patterned *via* e-beam lithography for etching. The patterned samples for the edge-contacted devices were etched for 30 s at a power of 30

DOI: 10.1021/acsnano.9b05965
ACS Nano 2019, 13, 13169−13175

W, with SF_6 gas at a flow rate of 10 sccm. Then, the used PMMA was removed using acetone and isopropanol, and fresh PMMA was spin-coated again to form electrode patterns. After the e-beam lithography, electrodes were formed by depositing 10-nm-thick layers of contact metals (Mn, Cr, and Au) and a 50-nm-thick layer of Au to obtain different metal contacts.

Characterization. Electrical transport measurements, including temperature-dependent characterization, were performed using a probe station and source/measurement units (Keithley 4200) under high-vacuum conditions (10^{-6} Torr).

ASSOCIATED CONTENT

Supporting Information

The Supporting Information is available free of charge on the ACS Publications website at DOI: 10.1021/acsnano.9b05965.

EDS mapping image; $I_{DS}-V_{BG}$ characteristics of TCMs of Mn and Au contacts; annealing effect on $I_{DS}-V_{BG}$ characteristics of ECM with Au; $I_{DS}-V_{BG}$ characteristics of ECM with Cr; calculation of band-bending profiles of MoS_2, ECM/TCM, and carrier concentration; band-bending plot for the ECM and TCM; FLP in the TCM for different values of L_T; extraction of the Schottky barrier height for monolayer-thick ECM with Au; contact resistivity of a 4.6-nm-thick ECM with Mn; schematic of the device fabrication process and optical images of the ECM (PDF)

AUTHOR INFORMATION

Corresponding Authors

*E-mail: ibhmoon@skku.edu.
*E-mail: leeyoung@skku.edu.

ORCID

Seok Joon Yun: 0000-0002-8695-7166
Young Hee Lee: 0000-0001-7403-8157

Author Contributions

§H. Choi and B. H. Moon contributed equally to this work.

Notes

The authors declare no competing financial interest.

ACKNOWLEDGMENTS

This work was supported by the Institute for Basic Science (IBS-R011-D1).

REFERENCES

(1) Wang, L.; Meric, I.; Huang, P. Y.; Gao, Q.; Gao, Y.; Tran, H.; Taniguchi, T.; Watanabe, K.; Campos, L. M.; Muller, D. A.; Guo, J.; Kim, P.; Hone, J.; Shepard, K. L.; Dean, C. R. One-Dimensional Electrical Contact to a Two-Dimensional Material. *Science* **2013**, *342*, 614−617.

(2) Radisavljevic, B.; Radenovic, A.; Brivio, J.; Giacometti, V.; Kis, A. Single-Layer MoS_2 Transistors. *Nat. Nanotechnol.* **2011**, *6*, 147−150.

(3) Wang, Q. H.; Kalantar-Zadeh, K.; Kis, A.; Coleman, J. N.; Strano, M. S. Electronics and Optoelectronics of Two-Dimensional Transition Metal Dichalcogenides. *Nat. Nanotechnol.* **2012**, *7*, 699−712.

(4) Jariwala, D.; Sangwan, V. K.; Lauhon, L. J.; Marks, T. J.; Hersam, M. C. Emerging Device Applications for Semiconducting Two-Dimensional Transition Metal Dichalcogenides. *ACS Nano* **2014**, *8*, 1102−1120.

(5) Popov, I.; Seifert, G.; Tomanek, D. Designing Electrical Contacts to MoS_2 Monolayers: A Computational Study. *Phys. Rev. Lett.* **2012**, *108*, 156802.

(6) Das, S.; Chen, H. Y.; Penumatcha, A. V.; Appenzeller, J. High Performance Multilayer MoS_2 Transistors with Scandium Contacts. *Nano Lett.* **2013**, *13*, 100−105.

(7) Qiu, H.; Pan, L. J.; Yao, Z. N.; Li, J. J.; Shi, Y.; Wang, X. R. Electrical Characterization of Back-Gated Bi-Layer MoS_2 Field-Effect Transistors and the Effect of Ambient on their Performances. *Appl. Phys. Lett.* **2012**, *100*, 123104.

(8) Cui, X.; Shih, E. M.; Jauregui, L. A.; Chae, S. H.; Kim, Y. D.; Li, B. C.; Seo, D.; Pistunova, K.; Yin, J.; Park, J. H.; Choi, H. J.; Lee, Y. H.; Watanabe, K.; Taniguchi, T.; Kim, P.; Dean, C. R.; Hone, J. C. Low-Temperature Ohmic Contact to Monolayer MoS_2 by van der Waals Bonded Co/h-BN Electrodes. *Nano Lett.* **2017**, *17*, 4781−4786.

(9) Leong, W. S.; Gong, H.; Thong, J. T. L. Low-Contact-Resistance Graphene Devices with Nickel-Etched-Graphene Contacts. *ACS Nano* **2014**, *8*, 994−1001.

(10) Georgiou, T.; Jalil, R.; Belle, B. D.; Britnell, L.; Gorbachev, R. V.; Morozov, S. V.; Kim, Y. J.; Gholinia, A.; Haigh, S. J.; Makarovsky, O.; Eaves, L.; Ponomarenko, L. A.; Geim, A. K.; Novoselov, K. S.; Mishchenko, A. Vertical Field-Effect Transistor Based on Graphene-WS2 Heterostructures for Flexible and Transparent Electronics. *Nat. Nanotechnol.* **2013**, *8*, 100−103.

(11) Britnell, L.; Gorbachev, R. V.; Jalil, R.; Belle, B. D.; Schedin, F.; Mishchenko, A.; Georgiou, T.; Katsnelson, M. I.; Eaves, L.; Morozov, S. V.; Peres, N. M. R.; Leist, J.; Geim, A. K.; Novoselov, K. S.; Ponomarenko, L. A. Field-Effect Tunneling Transistor Based on Vertical Graphene Heterostructures. *Science* **2012**, *335*, 947−950.

(12) Moon, B. H.; Han, G. H.; Kim, H.; Choi, H.; Bae, J. J.; Kim, J.; Jin, Y.; Jeong, H. Y.; Joo, M. K.; Lee, Y. H.; Lim, S. C. Junction-Structure-Dependent Schottky Barrier Inhomogeneity and Device Ideality of Monolayer MoS_2 Field-Effect Transistors. *ACS Appl. Mater. Interfaces* **2017**, *9*, 11240−11246.

(13) Yang, Z.; Kim, C.; Lee, K. Y.; Lee, M.; Appalakondaiah, S.; Ra, C. H.; Watanabe, K.; Taniguchi, T.; Cho, K.; Hwang, E. A Fermi-Level-Pinning-Free 1D Electrical Contact at the Intrinsic 2D MoS_2−Metal Junction. *Adv. Mater.* **2019**, *31*, 1808231.

(14) Kim, C.; Moon, I.; Lee, D.; Choi, M. S.; Ahmed, F.; Nam, S.; Cho, Y.; Shin, H. J.; Park, S.; Yoo, W. J. Fermi Level Pinning at Electrical Metal Contacts of Monolayer Molybdenum Dichalcogenides. *ACS Nano* **2017**, *11*, 1588−1596.

(15) Gong, C.; Colombo, L.; Wallace, R. M.; Cho, K. The Unusual Mechanism of Partial Fermi Level Pinning at Metal-MoS_2 Interfaces. *Nano Lett.* **2014**, *14*, 1714−1720.

(16) Cowley, A.; Sze, S. Surface States and Barrier Height of Metal-Semiconductor Systems. *J. Appl. Phys.* **1965**, *36*, 3212−3220.

(17) Bampoulis, P.; van Bremen, R.; Yao, Q. R.; Poelsema, B.; Zandvliet, H. J. W.; Sotthewes, K. Defect Dominated Charge Transport and Fermi Level Pinning in MoS_2/Metal Contacts. *ACS Appl. Mater. Interfaces* **2017**, *9*, 19278−19286.

(18) Liu, Y.; Guo, J.; Zhu, E. B.; Liao, L.; Lee, S. J.; Ding, M. N.; Shakir, I.; Gambin, V.; Huang, Y.; Duan, X. F. Approaching the Schottky-Mott Limit in van der Waals Metal-Semiconductor Junctions. *Nature* **2018**, *557*, 696−700.

(19) Natan, A.; Kronik, L.; Haick, H.; Tung, R. T. Electrostatic Properties of Ideal and Non-Ideal Polar Organic Monolayers: Implications for Electronic Devices. *Adv. Mater.* **2007**, *19*, 4103−4117.

(20) Tung, R. T. Formation of an Electric Dipole at Metal-Semiconductor Interfaces. *Phys. Rev. B: Condens. Matter Mater. Phys.* **2001**, *64*, 205310.

(21) Leonard, F.; Tersoff, J. Role of Fermi-Level Pinning in Nanotube Schottky Diodes. *Phys. Rev. Lett.* **2000**, *84*, 4693−4696.

(22) Han, S. W.; Kwon, H.; Kim, S. K.; Ryu, S.; Yun, W. S.; Kim, D. H.; Hwang, J. H.; Kang, J. S.; Baik, J.; Shin, H. J.; Hong, S. C. Band-Gap Transition Induced by Interlayer van der Waals Interaction in MoS_2. *Phys. Rev. B: Condens. Matter Mater. Phys.* **2011**, *84*, 045409.

(23) Zhang, Y.; Li, H.; Wang, H.; Xie, H.; Liu, R.; Zhang, S.-L.; Qiu, Z.-J. Thickness Considerations of Two-Dimensional Layered Semiconductors for Transistor Applications. *Sci. Rep.* **2016**, *6*, 29615.

DOI: 10.1021/acsnano.9b05965
ACS Nano 2019, 13, 13169−13175

(24) Zhang, Y. J.; Ye, J. T.; Matsuhashi, Y.; Iwasa, Y. Ambipolar MoS2 Thin Flake Transistors. *Nano Lett.* **2012**, *12*, 1136−1140.
(25) Giannazzo, F.; Fisichella, G.; Greco, G.; Di Franco, S.; Deretzis, I.; La Magna, A.; Bongiorno, C.; Nicotra, G.; Spinella, C.; Scopelliti, M.; Pignataro, B.; Agnello, S.; Roccaforte, F. Ambipolar MoS_2 Transistors by Nanoscale Tailoring of Schottky Barrier Using Oxygen Plasma Functionalization. *ACS Appl. Mater. Interfaces* **2017**, *9*, 23164−23174.
(26) Chen, M. K.; Nam, H.; Wi, S. J.; Ji, L.; Ren, X.; Bian, L. F.; Lu, S. L.; Liang, X. G. Stable Few-Layer MoS_2 Rectifying Diodes Formed by Plasma-Assisted Doping. *Appl. Phys. Lett.* **2013**, *103*, 142110.
(27) Siao, M. D.; Shen, W. C.; Chen, R. S.; Chang, Z. W.; Shih, M. C.; Chiu, Y. P.; Cheng, C. M. Two-Dimensional Electronic Transport and Surface Electron Accumulation in MoS_2. *Nat. Commun.* **2018**, *9*, 1442.
(28) Li, S. L.; Wakabayashi, K.; Xu, Y.; Nakaharai, S.; Komatsu, K.; Li, W. W.; Lin, Y. F.; Aparecido-Ferreira, A.; Tsukagoshi, K. Thickness-Dependent Interfacial Coulomb Scattering in Atomically Thin Field-Effect Transistors. *Nano Lett.* **2013**, *13*, 3546−3552.
(29) Das, S.; Appenzeller, J. Where Does the Current Flow in Two-Dimensional Layered Systems? *Nano Lett.* **2013**, *13*, 3396−3402.
(30) Tung, R. T. Recent Advances in Schottky Barrier Concepts. *Mater. Sci. Eng., R* **2001**, *35*, 1−138.
(31) Chen, X. L.; Wu, Z. F.; Xu, S. G.; Wang, L.; Huang, R.; Han, Y.; Ye, W. G.; Xiong, W.; Han, T. Y.; Long, G.; Wang, Y.; He, Y. H.; Cai, Y.; Sheng, P.; Wang, N. Probing the Electron States and Metal-Insulator Transition Mechanisms in Molybdenum Disulphide Vertical Heterostructures. *Nat. Commun.* **2015**, *6*, 6088.
(32) Guo, Y. Z.; Liu, D. M.; Robertson, J. 3D Behavior of Schottky Barriers of 2D Transition-Metal Dichalcogenides. *ACS Appl. Mater. Interfaces* **2015**, *7*, 25709−25715.
(33) Anwar, A.; Nabet, B.; Culp, J.; Castro, F. Effects of Electron Confinement on Thermionic Emission Current in a Modulation Doped Heterostructure. *J. Appl. Phys.* **1999**, *85*, 2663−2666.
(34) Zhou, Y.; Han, W.; Wang, Y.; Xiu, F. X.; Zou, J.; Kawakami, R. K.; Wang, K. L. Investigating the Origin of Fermi Level Pinning in Ge Schottky Junctions Using Epitaxially Grown Ultrathin MgO Films. *Appl. Phys. Lett.* **2010**, *96*, 102103.
(35) Chen, J. R.; Odenthal, P. M.; Swartz, A. G.; Floyd, G. C.; Wen, H.; Luo, K. Y.; Kawakami, R. K. Control of Schottky Barriers in Single Layer MoS_2 Transistors with Ferromagnetic Contacts. *Nano Lett.* **2013**, *13*, 3106−3110.
(36) Appenzeller, J.; Radosavljevic, M.; Knoch, J.; Avouris, P. Tunneling *versus* Thermionic Emission in One-Dimensional Semiconductors. *Phys. Rev. Lett.* **2004**, *92*, 048301.
(37) Das, S.; Appenzeller, J. Screening and Interlayer Coupling in Multilayer MoS_2. *Phys. Status Solidi RRL* **2013**, *7*, 268−273.
(38) Zhang, P.; Lau, Y. Y.; Gilgenbach, R. M. Analysis of Current Crowding in Thin Film Contacts from Exact Field Solution. *J. Phys. D: Appl. Phys.* **2015**, *48*, 475501.

DOI: 10.1021/acsnano.9b05965
ACS Nano 2019, 13, 13169−13175